scientific reports

Check for updates

OPEN

Delayed subsidence of the Dead Sea shore due to hydro-meteorological changes

Sibylle Vey[1]✉, D. Al-Halbouni[1,2], M. Haghshenas Haghighi[3], F. Alshawaf[1], J. Vüllers[4], A. Güntner[1,5], G. Dick[1], M. Ramatschi[1], P. Teatini[6], J. Wickert[1,7] & M. Weber[1]

Many studies show the sensitivity of our environment to manmade changes, especially the anthropogenic impact on atmospheric and hydrological processes. The effect on Solid Earth processes such as subsidence is less straightforward. Subsidence is usually slow and relates to the interplay of complex hydro-mechanical processes, thus making relations to atmospheric changes difficult to observe. In the Dead Sea (DS) region, however, climatic forcing is strong and over-use of fresh water is massive. An observation period of 3 years was thus sufficient to link the high evaporation (97 cm/year) and the subsequent drop of the Dead Sea lake level (– 110 cm/year), with high subsidence rates of the Earth's surface (– 15 cm/year). Applying innovative Global Navigation Satellite System (GNSS) techniques, we are able to resolve this subsidence of the "Solid Earth" even on a monthly basis and show that it behaves synchronous to atmospheric and hydrological changes with a time lag of two months. We show that the amplitude and fluctuation period of ground deformation is related to poro-elastic hydro-mechanical soil response to lake level changes. This provides, to our knowledge, a first direct link between shore subsidence, lake-level drop and evaporation.

Motivation

The Dead Sea is a hyper-saline terminal lake located in the Dead Sea transform rift system[1–3]. Today its catchment area provides fresh water for more than 16 million people in Jordan, Israel and the Palestinian territories[4]. In recent decades, this region has faced substantial environmental challenges[5]; water scarcity is one of the most serious. Since the 1950s, anthropogenic influence led to an unprecedented recession of the Dead Sea[4–6]. The lake level has steadily decreased with now more than – 110 cm/year[7], leaving the level in October 2018 at 433 m below mean sea-level (msl).

There are several reasons for the net loss of lake volume in the water balance of the Dead Sea[5,8]: (1) A high net evaporation rate of around 1000 mm/year (~ $700 \times 10e6$ m^3/year) with large seasonal variations[9] of which the quantification has recently been improved by new eddy covariance measurements[10]; (2) Extensive use of the DS brine for Potash production in Israel and Jordan with a net water usage in the order of 250×10^6 m^3/year is estimated to be responsible for 40% of the lake level drop[8,11]; (3) Large water irrigation projects in the North[12], causing fresh water inflow of the Jordan River to decrease by 90% compared to the natural situation before 1955, to $60–400 \times 10e6$ m^3/year nowadays[11,13,14].

Generally, surface and subsurface water inflow into the Dead Sea are difficult to determine due to complex geology and spatio-temporal effects[8,15–17]. Regional-scale 3D hydro(geo)logical modelling in salt-water environments has shown the most promising results for the Dead Sea aquifer systems[18–21]. Water inflow into the DS comprises direct surface runoff from river basins with a volume of $58–66 \times 10^6$ m^3/year (excluding the Jordan River), submarine groundwater discharge for the Lower Cretaceous Aquifers of ca. $170 \times 10e6$ m^3/year and precipitation on the lake surface of ca. 45×10^6 m^3/year[8,11]. These inflows, which additionally tend to decrease due to climate change[21–23] cannot compensate for the high evaporation.

The rapid decline of the DS level leads to both short and medium term climatic changes and natural hazards[5,24,25] that pose a major challenge to local communities[26]. Changes in precipitation and evaporation cause major flooding events, desertification and land degradation[4,26,27]. The retreat of the salt-water to fresh-water transition zone at the DS shore[28] results in an increasing groundwater gradient[7,29]. Both developments have led

[1]Deutsches GeoForschungsZentrum, GFZ, Telegrafenberg, 14473 Potsdam, Germany. [2]GEOMAR - Helmholtz Centre for Ocean Research, Kiel, Germany. [3]Leibniz University Hanover, Hanover, Germany. [4]Karlsruhe Institute of Technology, Karlsruhe, Germany. [5]University of Potsdam, Potsdam, Germany. [6]University of Padova, Padua, Italy. [7]Technische Universität Berlin, Berlin, Germany. ✉email: sibylle.vey@gfz-potsdam.de

to dissolution and erosion processes of the DS sediments, evaporates (salt) and other soluble material on both sides of the Dead Sea[30–32]. As a consequence, strong subsidence in the order of mm to cm/month on different spatial scales[7,33–35] and hazardous local sinkhole phenomena occur[30,31,36], with disastrous effects on infrastructure, industry, tourism and agriculture[6,37,38].

Determining the link between land subsidence and lake level change is essential for understanding the physical processes behind. Subsidence estimation at the Dead Sea has been performed locally by close-range photogrammetry, interferometric synthetic aperture radar (InSAR) or LiDAR techniques or by reconstruction of the Dead Sea bathymetry[7,33,34,36,39–43]. In contrast, regional studies exist that yield contrasting results, interpreted as lithostatic rebound[46].

To shed light on the link between evaporation rate, lake-level decline and ground subsidence we use a recently acquired and compiled dataset in the framework of the interdisciplinary DESERVE (DEad SEa Research VEnue) project[5]. Ground deformation is hereby measured with up-to-date high precision Global Navigation Satellite System (GNSS) stations. GNSS reflectometry is used for high precision leveling. GNSS is especially suitable for monitoring high temporal land subsidence variations as expected in natural and man-made (mining) cases e.g. Refs.[45–48]. We use this technique to record the temporal subsidence at the western side of the Dead Sea, in different distances to the shore line. We compare, in high temporal resolution, evaporation and lake level changes at the Dead Sea and are able to determine a first direct and interdisciplinary link on a monthly basis between the Solid Earth, climate and water processes.

Study area and experiment description

Figure 1 shows the tectonic setting of the DS and the location of the Global Navigation Satellite System (GNSS) stations used. The study area is located on the west coast of the DS near Ein Gedi, Israel, at 31.41° N, 35.39° E. Meteorological and GNSS data were recorded for nearly 3 years from 11th June 2014 until 29th March 2017. The SPA site had a fixed location next to the spa area of Ein Gedi. As the coastline of the DS retreats about 100 m/year horizontally, the Beach site had to be moved twice towards the waterfront in spring 2015 and 2016, respectively. The GNSS antennas are mounted about 4 m above the ground on towers with meteorological sensors (tipping bucket rain gauge 52,202 from Young IRGASON; integrated CO_2/H_2O open-path gas analyzer and 3D sonic anemometer from Campbell Scientific) installed by the Karlsruhe Institute of Technology (KIT) in the framework of the DESERVE project[5]. The GNSS equipment consists of an OEM receiver board type Javad TRE_G3T and an antenna Javad JAV_GRANT-G3T without radome. The ground around the Beach station is a slightly undulating, massive and rock-hard salt crust of 10–20 cm thickness (Fig. 1b). Below this stable lid of salt, the soft clayey sediments are brine-/water-logged. GNSS-reflectometry, a method that uses the GNSS signals reflected from land, snow and water surfaces is applied to monitor the Dead Sea lake level change[49–54]. For details on the data analysis and the construction of 3-year GNSS time series, the reader is referred to the supplement and Supplementary Figs. S_1 and S_2, respectively.

Observations

To validate the GNSS reflectometry method, we compare the GNSS derived DS lake level with gauge measurements near Massada (31.32863 N, 35.40299 E) from the Hydrological Service and Water Authority in Israel, for the 3-year observation period (Fig. 2). The mean deviation between the DS lake level from gauge observations and the lake level derived from GNSS reflectometry is ± 2.7 cm. The correlation coefficient of 0.99 ± 0.001 indicates an excellent accuracy and robustness of the GNSS method. The linear trend for the 3-year observation period (2014–2017) of the DS lake is − 110 ± 7 cm/year.

Figure 3 shows the vertical movement of the land surface at the SPA and Beach stations for the whole observation period. The standard error per month is ± 1.1 cm and the average subsidence is − 2.4 ± 0.7 cm/year and − 15.3 ± 1.2 cm/year at the SPA and Beach stations, respectively. The subsidence at the Beach station derived from InSAR corresponds with − 15.9 ± 1.5 cm/year very well to the GNSS observations. The spatial distribution of the subsidence between the Beach and the SPA stations is shown in the supplementary material for InSAR images (Supplementary Fig. S_4).

Seasonal variation of subsidence

To isolate the seasonal signal of the lake level drop and of beach subsidence from the general trend we remove the 3-year trend from the data. The Beach station shows a seasonal signal in the subsidence while the SPA station does not (Fig. 4). Positive anomalies of the overall decreasing DS lake level trend (positive numbers in Fig. 4a) are related to precipitation and less evaporation in the winter months. Anthropogenic water usage also plays a role and is discussed below. The main subsidence at the Beach site occurs from May to January (given as an anomaly of − 1.3 cm/month relative to the long-term subsidence in Fig. 4a), whereas it is significantly smaller from January to May (anomaly of 0.5 cm/month). The subsidence at the beach shows the highest correlation (0.84) with the DS lake level for a delay of two months (see Supplementary Fig. S_3), see also insert in Fig. 4a.

Figure 4b shows the subsidence of the beach, the lake level and the accumulated evaporation determined from data recorded at the same meteorological tower on which the GNSS antenna was mounted[10]. For details see supplement and Supplementary Fig. S_3. High correlations between evaporation/lake level and subsidence are expected since the fine-grained sediments cause complete consolidation quickly[33,55]. The scaling factor between absolute lake level change and subsidence is 7.2 (Fig. 4b). This means that the beach drops—with a time delay of 2 months—with the lake level, but at a 7.2 times smaller rate.

The lake level drop (− 110 cm/year) is larger than the evaporation observed at this location (97 cm/year). Firstly, this is due to the fact that the inflow of the Jordan river is massively reduced through overuse for consumption and that secondly the brines of the DS are used by industry ~ 30 km south of our observation point[5,8,11].

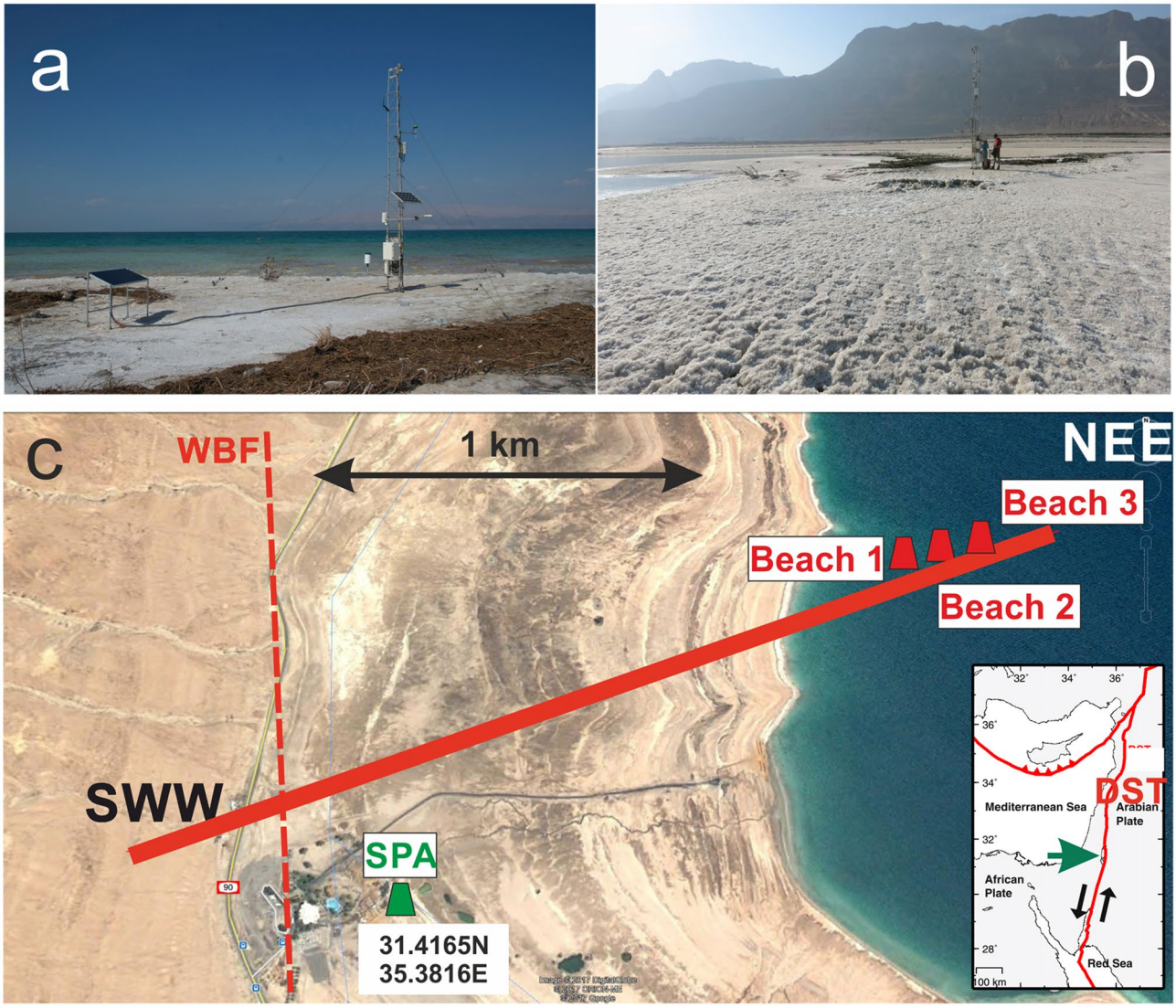

Figure 1. (**a**) GNSS station in June 2014 (Beach 1). (**b**) GNSS station in December 2014 (Beach 1). (**c**) Study area at the Dead Sea (DS) near Ein Gedi, Israel, with the four GNSS observation sites as green (SPA, with coordinates) and red (Beach) symbols, respectively. The solid red line shows the profile in Fig. 5 (2.4 km length). Note that the Google image is from 2010. In 2014, the DS had sufficiently receded so that the Beach 1 station was on land. This station had then to be moved twice to be near the lakeshore. *WBF* Western Boundary Fault (dashed line), a fault of the Dead Sea Transform (DST) system. (Insert) Study area at the DS (green arrow). Black arrows indicate the left lateral displacement of 105 km at the DST[27]. Image © 2017 Digital Globe, © 2017 ORION-ME, © 2017 Google.

The sum of evaporation losses and of water withdrawals for the potash production, which amount to close to half of the evaporation losses, cannot be compensated by the surface and subsurface inflow to the DS and cause the long-term decline of its water table[3].

Discussion

Origin of land subsidence. Land subsidence at the Dead Sea region occurs on different spatial and temporal scales[7]:

(1) Meter to decimeter scale sinkholes are related to subsurface material dissolution and mechanical mobilization[30,32] either due to dissolution of a salt edge[56,57], structurally controlled groundwater percolation[58,59] or subsurface stream channels[36,60,61] Formation rates vary hereby from sudden (e.g. within seconds) or in the order of mm-cm/month as determined by photogrammetric/InSAR/LiDAR studies[34,36,40,41,44] and morphologies of such sinkholes vary according to mechanical properties of the overburden[66,67].

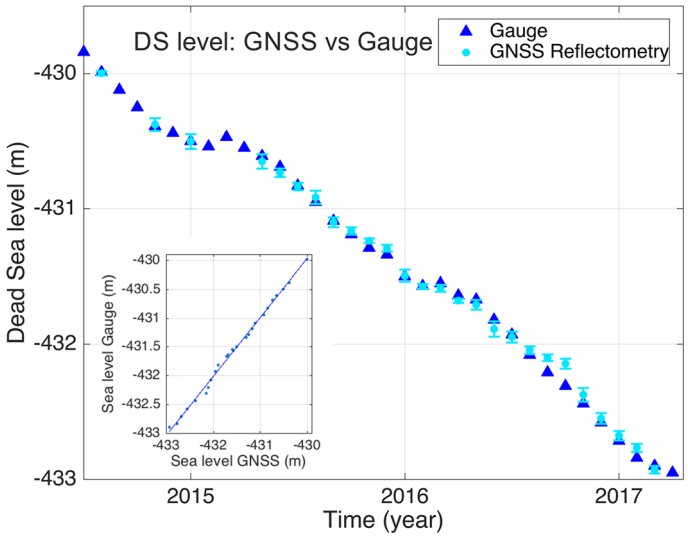

Figure 2. Blue triangles represent the DS lake level from 11th June 2014 to 29th March 2017, in meters below mean sea level, data provided by the Hydrological Service and Water Authority, Israel (Gauge near Massada). The DS lake level determined from GNSS reflectometry observations (Fig. 1, Beach stations) is shown in light blue (dots), with error bars. The standard error of the GNSS measurements is ± 2.7 cm. (Insert) The correlation coefficient between the two time series is 0.99, indicating the high accuracy of the GNSS observations.

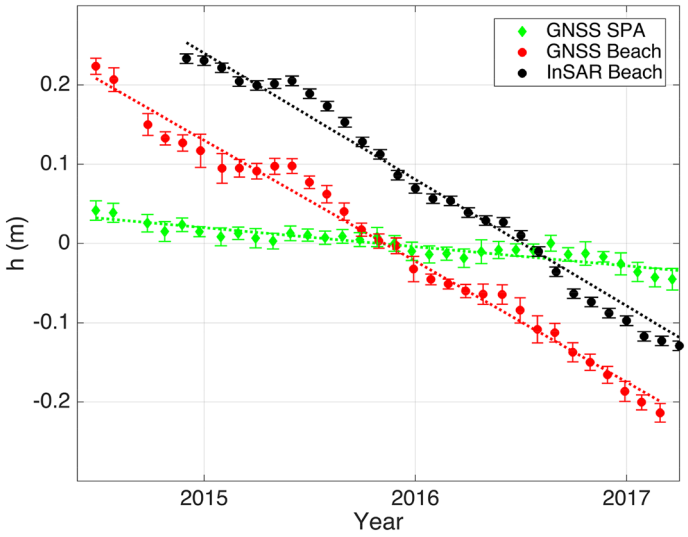

Figure 3. Displacement relative to the middle of the observation period is shown for the GNSS station at the SPA (green symbols) and the Beach stations (red symbols), respectively, between June 2014 and March 2017, in meters. The average subsidence at the SPA is − 2.4 ± 0.7 cm/year that at the beach is − 15.3 ± 1.2 cm/year, respectively. The standard error of the monthly mean GNSS height measurements is ± 1.1 cm. The subsidence at the beach derived from InSAR is − 15.9 ± 1.5 cm/year.

(2) Hundred meter scale depressions as common karstic landforms, so called uvalas[62], usually with sinkhole formation in parallel or earlier than the depressions with a strong temporal relation to base-level fall and structural trends as well as the fresh-salt-water boundary[7,58,59].

(3) A large-scale distributed non-linear subsidence with rates between 0.01 and 0.3 m/year depending on the distance towards the shoreline[7]. The rates agree well with previous InSAR or photogrammetric studies[33,41,43], including the results presented in this study. Effects of subsurface channel or local dissolution related subsidence close to or above active channels can be ruled out for the study site discussed here, as we observe rather opposite patterns of seasonal subsidence variation compared to[42]. The nearest visible surface channel is in a distance of ~ 750 m and the nearest sinkholes are reported to occur several hundreds of meters to the north and west of the Beach station[35,63], and also a few hundred meters from the SPA station. Given the typical size distribution of sinkholes in clayey marl/alluvial sediments[36,40], ground subsidence due to

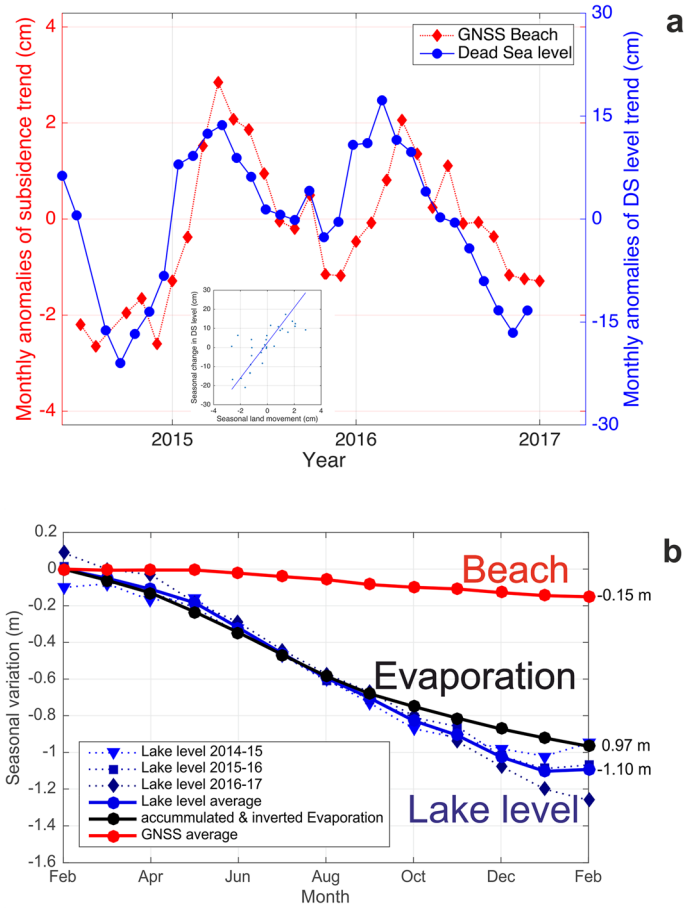

Figure 4. (**a**) Monthly anomalies of the subsidence of the Beach station (red, from GNSS) and of the drop of the lake level of the DS (blue, gauge) from June 2014 to March 2017, after removal of their respective 3-year trends (− 15.3 cm/year and − 110 cm/year). The standard error for the subsidence anomalies is ± 1.1 cm and for the lake level anomalies is ± 2.7 cm. (Insert) Correlation between the two time series after backward shifting of the subsidence time series by 2 months, with a correlation coefficient of 0.84 (see also Supplementary Fig. S_3). (**b**) Absolute values for Beach subsidence (red), lake level drop (blue) and evaporation (black), respectively, for three 12-month periods from February to February (2014/2015, 2015/2016, 2016/2017). The solid lines depict the respective average over the three years; the dashed lines are the values for the single years. The winter 2014/2015 was wet (see Supplementary Fig. S_6) and that of 2016/2017 was dry, both visible in higher or lower lake level values, respectively. The values for the cumulative evaporation are based on Ref.[10]. The scaling factor between Beach (land) and the DS lake level is 7.2; i.e. − 100 cm DS lake level decrease corresponds to − 13.9 cm sinking of the beach.

sinkholes would not be observed in the footprint area (Fresnel zones) of the GNSS antenna for our study sites (see Supplementary Information). Also, uvala formation in either cover material is usually accompanied by large-scale crack formation[7], something not observed for the area close to the GNSS stations.

Soil mechanics considerations. The formation of subsidence generally depends also on the rock/soil mechanical properties, as highlighted in various numerical modelling studies from Refs.[39,64–67]. A drop in pore pressure due to the decline of the lake level and, thus, in the fine-grained sediments along the shoreline, causes the sediments to consolidate[33]. The main subsurface material in the area is clayey marl and dewatering is a complex process involving kinetic, thermodynamic and electrochemical aspects[68]. Broad-scale subsidence along the DS shoreline has been attributed to such compaction of fine-grained formerly water-logged sediments, and was estimated to several cm/year for marl deposits of the study area by analytical considerations[33]. The sediments of the Dead Sea, alluvium, clayey marl deposits and salt, have distinguished mechanical strengths and behavior ranging from brittle- to ductile failure[53,64,68,69], and salt concentration of water-clogged sediments has a significant influence on shear strength and Atterberg limits[70]. In combination with the above-mentioned missing evidence of sinkhole and uvala formation, we therefore consider option (3) from above, the large-scale compaction of the former Dead Sea lake-bed, as the most probable process that causes the observed subsidence.

We present analytical calculations of ground subsidence and water level fluctuation propagation by applying simple analytical 1D-soil compaction theory based on Refs.[71,72]. This assumes, for simplicity, a 20 m thick

unconfined, isotropic, homogeneous and fully saturated Dead Sea brine layer of marl overlying a thick Holocene salt layer. For a water-level decrease of 1.1 m (corresponding to the mean annual Dead Sea water level decline, see Fig. 4b), the results show a 1D solid consolidation of 10.2–17.0 cm with a primary consolidation time of 1.2–3.6 years. The observed values at the station Beach are within this range. Further details on the analysis and assumptions made can be found in the supplement.

Delayed groundwater pressure propagation may be the primary reason for the observed time shift between DS lake-level drop and subsidence. In fact, assuming the aquifer system as a poro-elastic body, a seasonality of the subsurface fluid pressure causes a simultaneous behavior of soil deformation because of the effective stress fluctuation[71,73]. To test this hypothesis we used the 1D analytical poro-elastic response of an aquifer system subject to lake-level fluctuations. Specifically, the interest is to understand how the signal represented by the DS level after removal of the 3-year trend propagates inside the beach from the DS. Figure 4a suggests that this residual sea level fluctuation can be viewed as a long-term tide characterized by an amplitude of ca. $\zeta_0 = 15$ cm and a period $t_0 = 365$ days. We consider a homogeneous beach of a water saturated clayey marl characterized by an isotropic permeability, constant effective porosity, horizontal groundwater flow and hydrostatic conditions to solve the governing equations for effective stress calculation based on poro-elasticity (see supplement). The distance of the Beach station to the water ranged from 10 to 35 m during the survey time. Using these values yields a time-lag of level drop propagation between $t_L = 29$ days and $t_L = 101$ days, respectively, which encompass the estimated time shift between the observed DS level and land movement at Beach station (ca. 60 days). Taking advantage of the previous soil mechanical computation, we can use the ratio between the yearly DS level change and the shore land displacement, i.e. $r = 7.2$, to make a rough estimate of the possible seasonal movement above the Beach station due to the inland propagation of the seasonal sea level fluctuation. We obtain a value equal to 1.25 cm for 10 m distance from the shoreline, and 1.98 cm for 1 m distance, close to the average value ~ 2 cm, as shown in Fig. 4a. At more than 35 m distance from the shoreline the seasonal displacement becomes negligible. With the background of the fast regression of the shoreline and related exposure of the Dead Sea clayey marl, theoretical and measured values are in good agreement.

This cause-and-effect behavior has been already observed above underground gas storage reservoirs[74], alluvial confined aquifers cyclically exploited[75], and fractured rock aquifers experiencing Earth tides[76]. Recently, albeit for different hydrogeological settings, a time lag of about 45 days between surface displacements and variations of the groundwater level was published[77], in line with the observations obtained here. However, to our knowledge, it is the first time that this has been directly recorded on a shore.

We would like to point out, however, that variations of compression indices and coefficients of consolidation with time, Atterberg limits and pre-consolidation pressure were not considered in the consolidation calculations. Also, 3D effects and non-homogeneous soils, e.g., with respect to their lime content[78], may play a role and have not been considered here. The general lack of similar high-frequency subsidence data prevents us from assessing our results in a broader context. Spatially varying layer depths, material heterogeneity and liquefaction, and the groundwater-fresh water interface locally penetrated by subsurface conduits are responsible for the different magnitudes of large-scale subsidence along the Dead Sea shoreline[7] and also for a location-dependent time lag between water level drop and subsidence. For analyzing these effects more accurately, longer high-resolution measurements on several locations along the Dead Sea would be necessary. Nevertheless, the values observed at the Beach site show a valuable first benchmark for the rate of subsidence by poro-elastic consolidation of silt and clay sediments along the DS shoreline, which is highly uncertain due to the difficulties to determine sediment properties[55].

Hydrogeological and tectonic considerations. The high correlation (0.99) between the average annual beach subsidence (red in Fig. 4a) and lake level drop (blue) and the cumulative evaporation (black; correlation coefficient − 0.97), respectively, shows the close connection of the processes in these three spheres. Away from the shore (ca. 2 km west), the subsidence at the SPA station (− 2.4 cm/year) is much smaller (Fig. 5, green symbols). This small subsidence rate could be explained by the overlay of a residual hydrology-induced subsidence (the beach receded from this location more than 35 years ago, but the groundwater table still declines in the deeper subsurface, compaction goes on and, thus, subsidence can be expected to continue at small rates) and the tectonically driven subsidence of the DS basin of up to 0.3 mm/year[79]. Furthermore, the decline of the groundwater table as a consequence of receding lake levels tends to decrease with the distance from the shoreline[31,80]. The associated compaction of fine sediments and, thus, subsidence may be more pronounced close to the shoreline.

A regional process that affects the hydrology at the western shores of the DS is the varying groundwater inflow from the recharge areas in the mountains towards the west[31]. Due to long travel and residence times in the aquifer from the recharge areas to the DS, the seasonality of rainfall and recharge is fully dampened out in the inflow to the DS area[31]. Thus, an impact of regional groundwater flow on the seasonality of lake level and subsidence observed in this study can most likely be ruled out.

West of the Western Boundary Fault (WBF), see Fig. 1, no vertical displacement is detectable (see Supplement Information and Supplementary Figs. S_4 and S_5). The vertical subsidence observed at the beach and its seasonal dynamics are clearly dominated by local hydrological processes in the sediments, which are in turn shaped by meteorological phenomena, like the wind systems dominating the evaporation processes; for details on the wind systems see Ref.[10].

Figure 5 summarizes the different phenomena (subsidence, lake level decline and evaporation). While the reaction chain of evaporation, lake level drop and beach subsidence is now established, the surprise is the high synchronicity—with a time lag of 2 months for the beach—of these observations, dominated by a seasonal cycle.

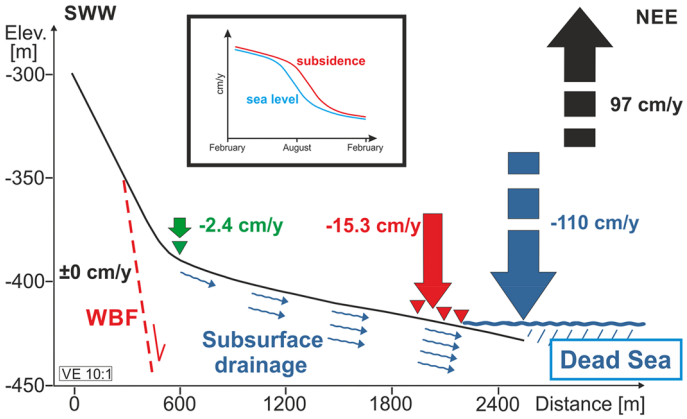

Figure 5. Sketch of the average yearly subsidence across the red profile shown in Fig. 1, from June 2014 to March 2017. The green and red triangles are the location of the GNSS stations. Green and red arrows indicate the subsidence of the surface. The area west of the WBF (Western Boundary Fault, dashed red line) shows no vertical movement (see Supplementary Figs. S_4 and S_5), whereas the subsidence increases from − 2.4 cm/year near the SPA to − 15.3 cm/year at the Beach. The main cause of the massive subsidence observed is the drainage of the sediments below the stable salt crust, due to the drop of the DS water table. Water and its movement are labeled in blue. The average drop of the DS lake level is 110 cm/year. Vertical exaggeration is 10:1. The insert is a sketch showing in a generalized way the intra-annual dynamics of DS lake level (blue) and the delayed subsidence (red) (winter to summer to winter).

Summary

The study presented here shows that the use of geophysical observation methods like GNSS reflectometry in combination with traditional techniques enables us to detect the close linkage of land subsidence with changes in lake level and climate factors such as evaporation. We demonstrate, to our knowledge, for the first time the direct link of atmospheric phenomena to Solid Earth processes using the common factor water and resolve the interplay of the spheres on a seasonal, respectively monthly basis. These dynamic processes, shaping the surface of our Earth, show the high vulnerability of our environment to complex chains of processes in the geo-sphere strongly driven by human activities.

Received: 23 January 2019; Accepted: 12 May 2021
Published online: 29 June 2021

References

1. Bender, F. *Geologie von Jordanien*. (ed. Gebrüder Bornträger), (Schweizerbart Science Publishers, Stuttgart, Germany, 1968).
2. Freund, R., Zak, I. & Garfunkel, Z. Age and rate of sinistral movement along Dead Sea rift. *Nature* **220**, 253 (1968).
3. Garfunkel, Z. & Ben-Avraham, Z. The structure of the Dead Sea basin. *Tectonophysics* **266**, 155–176 (1996).
4. Closson, D., Pasquali, P., Riccardi, P., Milisavljevic, N. & Abou Karaki, N. The water deficit in the Middle East and the disappearance of the Dead Sea. In *Desertification and Land Degradation—Processes and Mitigation* (eds De Boever, M. *et al.*) (UNESCO Chair of Eremology, 2013).
5. Kottmeier, C. *et al.* New perspectives on interdisciplinary earth science at the Dead Sea: The DESERVE project. *Sci. Total Environ.* **544**, 1045–1058. https://doi.org/10.1016/j.scitotenv.2015.12.003 (2016).
6. Abou Karaki, N., Fiaschi, S. & Closson, D. Sustainable development and anthropogenic induced geomorphic hazards in subsiding areas. *Earth Surf. Process. Landf.* **41**(15), 2282–2295. https://doi.org/10.1002/esp.4047 (2016).
7. Watson, R. A. *et al.* Sinkholes and uvalas in evaporite karst: spatio-temporal development with links to base-level fall on the eastern shore of the Dead Sea. *Solid Earth* **10**(4), 1451–1468. https://doi.org/10.5194/se-10-1451-2019 (2019).
8. Siebert, C. *et al.* Challenges to estimate surface- and groundwater flow in arid regions: The Dead Sea catchment. *Sci. Total Environ.* **485–486**, 828–841. https://doi.org/10.1016/j.scitotenv.2014.04.010 (2014).
9. Oroud, I. M. Evaporation estimates from the Dead Sea and their implications on its water balance. *Theor. Appl. Climatol.* **106**(3–4), 523–530. https://doi.org/10.1007/s00704-011-0452-6 (2011).
10. Metzger, J., Nied, M., Corsmeier, U., Kleffmann, J. & Kottmeier, C. Dead Sea evaporation by eddy covariance measurements versus aerodynamic, energy budget, Priestley-Taylor & Penman estimates. Hydrol. Earth Syst. Sci. https://doi.org/10.5194/hess-2017-187 (2017).
11. Lensky, N. G., Dvorkin, Y., Lyakhovsky, V., Gertman, I. & Gavrieli, I. Water, salt & energy balances of the Dead Sea. *Water Resour. Res.* **41**(12), 1–13. https://doi.org/10.1029/2005WR004084 (2005).
12. Gavrieli, I. & Oren, A. The Dead Sea as a dying lake. In *Dying and Dead Seas Climatic Versus Anthropic Causes SE—11* Vol. 36 (eds Nihoul, J. C. J. *et al.*) 287–305 (Springer, 2004).
13. Holtzman, R. *et al.* Quantifying ground water inputs along the Lower Jordan River. *J. Environ. Qual.* **34**, 897–906. https://doi.org/10.2134/jeq2004.0244 (2005).
14. Kiro, Y., Weinstein, Y., Starinsky, A. & Yechieli, Y. The extent of seawater circulation in the aquifer and its role in elemental mass balances: A lesson from the Dead Sea. *Earth Planet Sci. Lett.* **394**, 146–158. https://doi.org/10.1016/j.epsl.2014.03.010 (2014).
15. Siebert, C. *et al.* Multidisciplinary investigations of the transboundary Dead Sea basin and its water resources BT—Integrated water resources management: Concept. In *Research and implementation* (eds Borchardt, D. *et al.*) 107–127 (Springer International Publishing, 2016).

16. Khayat, S., Marei, A., Geyer, S. & Rödiger, T. Investigating the complex hydrogeological settings in the northeastern slope of the West Bank to the Jordan Graben (Malih and Jeftlik). *Euro Mediterr. J. Environ. Integr.* **3**(1), 32. https://doi.org/10.1007/s41207-018-0074-9 (2018).
17. Mallast, U. & Siebert, C. Combining continuous spatial and temporal scales for SGD investigations using UAV-based thermal infrared measurements. *Hydrol. Earth Syst. Sci.* **23**, 1375–1392, https://doi.org/10.5194/hess-23-1375-2019 (2019).
18. Gräbe, A. *et al.* Numerical analysis of the groundwater regime in the western Dead Sea escaprment, Israel + West Bank. *Environ. Earth Sci.* **69**, 571–585. https://doi.org/10.1007/s12665-012-1795-8 (2013).
19. Rödiger, T. *et al.* Multi-response calibration of a conceptual hydrological model in the semiarid catchment of Wadi al Arab, Jordan. *J. Hydrol.* **509**, 193–206. https://doi.org/10.1016/j.jhydrol.2013.11.026 (2014).
20. Rödiger, T. *et al.* Assessing anthropogenic impacts on limited water resources under semi-arid conditions: Three-dimensional transient regional modelling in Jordan. *Hydrogeol. J.* https://doi.org/10.1007/s10040-017-1601-5 (2017).
21. Odeh, T., Rödiger, T., Geyer, S. & Schirmer, M. Hydrological modelling of a heterogeneous catchment using an integrated approach of remote sensing, a geographic information system and hydrologic response units: The case study of Wadi Zerka Ma'in catchment area, north east of the Dead Sea. *Environ. Earth Sci.* **73**(7), 3309–3326. https://doi.org/10.1007/s12665-014-3627-5 (2015).
22. Menzel, L., Teichert, E. & Weiss, M. Climate change impact on the water resources of the semi-arid Jordan region. In *Proc. 3rd International Conference on Climate and Water, Helsinki*, 320–325 (2007).
23. Al-Omari, A., Salman, A. & Karablieh, E. The Red Dead Canal project: An adaptation option to climate change in Jordan. *Desalin. Water Treat.* **52**(13–15), 2833–2840. https://doi.org/10.1080/19443994.2013.819168 (2014).
24. Alpert, P., Jin, F. & Kitoh, A. *A World After Climate Change and Culture-Shift* (ed. Norwine, J.), 193–203, (Springer Netherlands, 2014).
25. Kishcha, P., Pinker, R. T., Gertman, I., Starobinets, B. & Alpert, P. Observations of positive sea surface temperature trends in the steadily shrinking Dead Sea. *Nat. Hazards Earth Syst. Sci.* **25**(11), 1–15. https://doi.org/10.5194/nhess-18-3007-2018 (2018).
26. Shafir, H. & Alpert, P. Regional and local climatic effects on the Dead-Sea evaporation. *Clim. Change* **105**(3–4), 455–468. https://doi.org/10.1007/s10584-010-9892-8 (2011).
27. Hochman, A., Mercogliano, P., Alpert, P., Saaroni, H. & Bucchignani, E. High-resolution projection of climate change and extremity over Israel using COSMO-CLM. *Int. J. Climatol.* **38**(14), 5095–5106. https://doi.org/10.1002/joc.5714 (2018).
28. Salameh, E. & El-Naser, H. The interface configuration of the fresh-/dead sea water—Theory and measurements. *Acta Hydrochim. Hydrobiol.* **28**, 323–328 (2000).
29. Kiro, Y., Yechieli, Y., Lyakhovsky, V., Shalev, E. & Starinsky, A. Time response of the water table and saltwater transition zone to a base level drop. *Water Resour. Res.* **44**(12), 1–15. https://doi.org/10.1029/2007WR006752 (2008).
30. Arkin, A. & Gilat, Y. Dead Sea sinkholes—an ever-developing hazard. *Environ. Geol.* **39**(7), 711–722 (2000).
31. Abelson, M. *et al.* Natural versus human control on subsurface salt dissolution and development of thousands of sinkholes along the Dead Sea coast. *J. Geophys. Res. Earth Surf.* https://doi.org/10.1002/2017JF004219 (2017).
32. Polom, U. *et al.* Shear wave reflection seismics yields subsurface dissolution and subrosion patterns: Application to the Ghor Al-Haditha sinkhole site, Dead Sea, Jordan. *Solid Earth* **9**, 1079–1098. https://doi.org/10.5194/se-9-1079-2018 (2018).
33. Baer, G. *et al.* The lowest place on Earth is subsiding—An InSAR (interferometric synthetic aperture radar) perspective. *Geol. Soc. Am. Bull.* **114**(1), 12–23. https://doi.org/10.1130/0016-7606(2002)114%3c0012:TLPOEI%3e2.0.CO;2 (2002).
34. Atzori, S., Antonioli, A., Salvi, S. & Baer, G. InSAR-based modeling and analysis of sinkholes along the Dead Sea coastline. *Geophys. Res. Lett.* **42**, 8383–8390. https://doi.org/10.1002/2015GL066053 (2015).
35. Yechieli, Y., Abelson, M. & Baer, G. Sinkhole formation and subsidence along the Dead Sea coast, Israel. *Hydrogeol. J.* **24**(3), 601–612. https://doi.org/10.1007/s10040-015-1338-y (2016).
36. Al-Halbouni, D. *et al.* Sinkholes, subsidence and subrosion on the eastern shore of the Dead Sea as revealed by a close-range photogrammetric survey. *Geomorphology* **285**, 305–324. https://doi.org/10.1016/j.geomorph.2017.02.006 (2017).
37. Closson, D., Abou Karaki, N. & Hallot, F. Landslides along the Jordanian Dead Sea coast triggered by the lake level lowering. *Environ. Earth Sci.* **59**(7), 1417–1430. https://doi.org/10.1007/s12665-009-0128-z (2009).
38. Salameh, E., Alraggad, M. & Amaireh, M. Degradation processes along the new northeastern shores of the Dead Sea. *Environ. Earth Sci.* **78**(5), 1–12. https://doi.org/10.1007/s12665-019-8155-x (2019).
39. Baer, G. *et al.* InSAR measurements and viscoelastic modeling of Sinkhole precursory subsidence: Implications for Sinkhole formation, early warning & sediment properties. *J. Geophys. Res. Earth Surf.* **123**(4), 678–693. https://doi.org/10.1002/2017JF004594 (2018).
40. Filin, S., Baruch, A., Avni, Y. & Marco, S. Sinkhole characterization in the Dead Sea area using airborne laser scanning. *Nat. Hazards* **58**(3), 1135–1154. https://doi.org/10.1007/s11069-011-9718-7 (2011).
41. Fiaschi, S., Abou Karaki, N., Pasquali, P., Riccardi, P. & Floris, M. The complex karst dynamics of the Lisan Peninsula revealed by 25 years of DInSAR observations. Dead Sea, Jordan. *ISPRS J. Photogramm. Remote Sens.* **130**, 358–369. https://doi.org/10.1016/j.isprsjprs.2017.06.008 (2017).
42. Shviro, M., Haviv, I. & Baer, G. High-resolution InSAR constraints on flood-related subsidence and evaporite dissolution along the Dead Sea shores: Interplay between hydrology and rheology. *Geomorphology* **293**, 53–68. https://doi.org/10.1016/j.geomorph.2017.04.033 (2017).
43. Nof, R. N. *et al.* SAR interferometry for sinkhole early warning and susceptibility assessment along the Dead Sea, Israel. *Remote Sens.* **11**(1), 89. https://doi.org/10.3390/rs11010089 (2019).
44. Nof, R. N. *et al.* Rising of the lowest place on Earth due to Dead Sea water-level drop: Evidence from SAR interferometry and GPS. *J. Geophys. Res. Solid Earth* **117**(5), 1–16. https://doi.org/10.1029/2011JB008961 (2012).
45. Conway, B. D. Land subsidence and earth fissures in south-central and southern Arizona, USA. *Hydrogeol. J.* **24**(3), 649–655. https://doi.org/10.1007/s10040-015-1329-z (2015).
46. Kersten, T., Timmen, L., Schön, S., Kobe, M., Gabriel, G. & Vogel, D. On integrated geodetic monitoring for sinkhole-induced surface deformation and mass dislocation. In *JISDM*, 1–8 (2016).
47. Del Soldato, M., Farolfi, G., Rosi, A., Raspini, F. & Casagli, N. Subsidence evolution of the Firenze-Prato-Pistoia plain (Central Italy) combining PSI and GNSS data. *Remote Sens.* **10**(7), 1–19. https://doi.org/10.3390/rs10071146 (2018).
48. Tao, T., Liu, J., Qu, X. & Gao, F. Real-time monitoring rapid ground subsidence using GNSS and Vondrak filter. *Acta Geophys.* **67**(1), 133–140. https://doi.org/10.1007/s11600-018-0230-2 (2019).
49. Löfgren, J. S., Haas, R. & Scherneck, H.-G. Sea level time series and ocean tide analysis from multipath signals at five GPS sites in different parts of the world. *J. Geodyn.* **80**, 66–80. https://doi.org/10.1016/j.jog.2014.02.012 (2014).
50. Vey, S. *et al.* Monitoring snow depth by GNSS reflectometry in built-up areas: A case study for Wettzell, Germany. *IEEE J. Sel. Top. Appl. Earth Observ. Remote Sens.* **9**(10), 4817–4823. https://doi.org/10.1109/JSTARS.2016.2516041 (2016).
51. Vey, S., Güntner, A., Wickert, J., Blume, Th. & Ramatschi, M. Long-term soil moisture dynamics derived from GNSS interferometric reflectometry: A case study for Sutherland, South Africa. *GPS Solut. V* **20**(4), 641–654. https://doi.org/10.1007/s10291-015-0474-0 (2016).
52. Santamaría-Gómez, A. & Watson, C. Remote leveling of tide gauges using GNSS reflectometry: Case study at Spring Bay, Australia. *GPS Solut.* **21**(2), 451–459. https://doi.org/10.1007/s10291-016-0537-x (2017).
53. Larson, K. M., Ray, R. D. & Williams, S. P. A ten year comparison of water levels measured with a geodetic GPS receiver versus a conventional tide gauge. *J. Atmos. Ocean Technol.* **34**(2), 295–307. https://doi.org/10.1175/JTECH-D-16-0101.1 (2017).

54. Siegfried, M. R., Medley, B., Larson, K. M., Fricker, H. A. & Tulaczyk, S. Snow accumulation variability on a west Antarctic ice stream observed with GPS reflectometry, 2007–2017. *Geophys. Res. Lett.* **44**(15), 7808–7816. https://doi.org/10.1002/2017GL074039 (2017).
55. Frydman, S., Charrach, J. & Goretsky, I. A geotechnical study of evaporitic, lacustrine sediments in the saline environment of the Dead Sea area. *Eng. Geol.* **181**, 309–322. https://doi.org/10.1016/j.enggeo.2014.08.028 (2014).
56. Frumkin, A., Ezersky, M. G., Al-Zoubi, A. S., Akkawi, E. & Abueladas, A.-R. The Dead Sea sinkhole hazard: Geophysical assessment of salt dissolution and collapse. *Geomorphology* **134**(1–2), 102–117. https://doi.org/10.1016/j.geomorph.2011.04.023 (2011).
57. Ezersky, M. G. & Frumkin, A. Fault—Dissolution front relations and the Dead Sea sinkhole problem. *Geomorphology* **201**, 35–44. https://doi.org/10.1016/j.geomorph.2013.06.002 (2013).
58. Abelson, M. *et al.* Nanoseismicity forecasts sinkhole collapse in the Dead Sea coast years in advance. *Geology* **46**(1), 1–4. https://doi.org/10.1130/G39579.1 (2018).
59. Charrach, J. Investigations into the Holocene geology of the Dead Sea basin. *Carbonates Evaporites* **0123456789**, 1–28. https://doi.org/10.1007/s13146-018-0454-x (2018).
60. Avni, Y. *et al.* Self-accelerated development of salt karst during flash floods along the Dead Sea Coast, Israel. *J. Geophys. Res. Earth Surf.* https://doi.org/10.1002/2014JF003275 (2016).
61. Al-Halbouni, D. *et al.* Dynamics of hydrological and geomorphological processes in evaporite karst at the Eastern Dead Sea—A multidisciplinary study. *Hydrol. Earth Syst. Sci. Discuss.* **25**, 3351–3395, https://doi.org/10.5194/hess-25-3351-2021 (2021).
62. Ćalić, J. Karstic uvala revisited: Toward a redefinition of the term. *Geomorphology* **134**(1–2), 32–42. https://doi.org/10.1016/j.geomorph.2011.06.029 (2011).
63. Ezersky, M. G., Legchenko, A., Eppelbaum, L. & Al-Zoubi, A. S. Overview of the geophysical studies in the Dead Sea coastal area related to evaporite karst and recent sinkhole development. *Int. J. Speleol.* **46**, 277–302. https://doi.org/10.5038/1827-806X.46.2.2087 (2017).
64. Shalev, E., Lyakhovsky, V. & Yechieli, Y. Salt dissolution and sinkhole formation along the Dead Sea shore. *J. Geophys. Res.* **111**(B3102), 1–12. https://doi.org/10.1029/2005JB004038 (2006).
65. Shalev, E. & Lyakhovsky, V. Viscoelastic damage modeling of sinkhole formation. *J. Struct. Geol.* **42**, 163–170. https://doi.org/10.1016/j.jsg.2012.05.010 (2012).
66. Al-Halbouni, D. *et al.* Geomechanical modelling of sinkhole development using Distinct Elements: Model verification for a single void space and application to the Dead Sea area. *Solid Earth* **9**, 1341–1373. https://doi.org/10.5194/se-2018-62 (2018).
67. Al-Halbouni, D. *et al.* Distinct element geomechanical modelling of the formation of sinkhole clusters within large-scale karstic depressions. *Solid Earth* **10**(4), 1219–1241. https://doi.org/10.5194/se-10-1219-2019 (2019).
68. Burst, J. F. Argillaceous sediment dewatering. *Annu. Rev. Earth Planet. Sci.* **4**(1), 293–318. https://doi.org/10.1146/annurev.ea.04.050176.001453 (1976).
69. Frydman, S., Charrach, J. & Goretsky, I. Geotechnical properties of evaporite soils of the Dead Sea area. *Eng. Geol.* **101**(3–4), 236–244. https://doi.org/10.1016/j.enggeo.2008.06.003 (2008).
70. Ismeik, M., Ashteyat, A. M. & Ramadan, K. Z. Stabilisation of fine-grained soils with saline water. *Eur. J. Environ. Civ. Eng.* **17**(1), 32–45. https://doi.org/10.1080/19648189.2012.720399 (2013).
71. Terzaghi, K. *Theoretical Soil Mechanics* (Wiley, 1943).
72. Terzaghi, K., Peck, R. B. & Mesri, G. *Soil Mechanics in Engineering Practice* (Wiley, 1996).
73. Verruijt, A. *Soil Mechanics* (Delft University of Technology, 2012).
74. Teatini, P. *et al.* Geomechanical response to seasonal gas storage in depleted reservoirs: A case study in the Po River basin, Italy. *J. Geophys. Res. Earth Surf.* **116**, F02002. https://doi.org/10.1029/2010JF001793 (2011).
75. Boni, R. *et al.* 3D groundwater flow and deformation modelling of Madrid aquifer. *J. Hydrol.* **585**, 124773. https://doi.org/10.1016/j.jhydrol.2020.124773 (2020).
76. Burbey, T. J., Hisz, D., Murdoch, L. C. & Zhang, M. Quantifying fractured crystalline-rock properties using well tests, earth tides and barometric effects. *J. Hydrol.* **414–415**, 317–328. https://doi.org/10.1016/j.jhydrol.2011.11.013 (2012).
77. Haghighi, M. H. & Motagh, M. Ground surface response to continuous compaction of aquifer system in Tehran, Iran: Results from a long-term multi-sensor InSAR analysis. *Remote Sens. Environ.* **221**, 534–550. https://doi.org/10.1016/j.rse.2018.11.003 (2019).
78. Salehi, M. & Sivakugan, N. Effects of lime-clay modification on the consolidation behavior of the dredged mud. *J. Waterw. Port Coast. Ocean Eng.* **135**(6), 251–258 (2009).
79. Bartov, Y., Agnon, A., Enzel, Y. & Stein, M. Late Quaternary faulting and subsidence in the central Dead Sea basin, Israel. *J. Earth Sci.* **55**(1), 18–31 (2006).
80. Yechieli, Y., Shalev, E., Wollman, S., Kiro, Y. & Kafri, U. Response of the Mediterranean and Dead Sea coastal aquifers to sea level variations. *Water Resour. Res.* **46**(12), 1–11 (2010).
81. Wessel, P. & Smith, W. H. F. New, improved version of the Generic Mapping Tool released. *EOS. Trans. Am. Geophys. Un.* **79**, 579 (1998).

Acknowledgements

The work presented here was supported by the German Helmholtz Gemeinschaft (HGF) and the Deutsches GeoForschungsZentrum Potsdam (GFZ) as part of the DESERVE project. We thank A. Agnon for correcting our faults, A. Brauer for comments to this manuscript and A. Siebert for her help in drafting figures, most of them created with the GMT software[81]. We thank the six reviewer and the editor for their detailed comments, that significantly improved our manuscript. We appreciate the many useful discussions with the members of the DESERVE team. We thank the Kibbutz Ein Gedi, the Dead Sea and Arava Science Center, and P. Gasch for their support during the fieldwork. Dead Sea lake level data were kindly provided by the Hydrological Service and Water Authority, Israel (http://www.water.gov.il/Hebrew/Water-Environment/Dead-Sea/Documents/deadsea-report-updated-01.10.2017.pdf). The instruments for the fieldwork were provided by the GFZ.

Author contributions

S.V. and M.W. wrote the main manuscript text and prepared most of the figures. D.A.-H. wrote the introduction and solid earth part. M.H.H. and F.A. prepared the InSAR analysis. G.D. carried out the GNSS positioning analyses. J.V. provided the analyzed meteorological data and the sea level data from gauges. A.G. was responsible for the hydrological part. M.R. and J.W. provided the photos in Fig. 1 and were responsible for the GNSS data collection in the field. D.A.-H. and P.T. carried out the analytical modelling. All authors reviewed the manuscript.

Funding

Open Access funding enabled and organized by Projekt DEAL. Deutsche Forschungsgemeinschaft (German Research Foundation), Grant No. 501100001659.

Competing interests
The authors declare no competing interests.

Additional information
Supplementary Information The online version contains supplementary material available at https://doi.org/10.1038/s41598-021-91949-y.

Correspondence and requests for materials should be addressed to S.V.

Reprints and permissions information is available at www.nature.com/reprints.

Publisher's note Springer Nature remains neutral with regard to jurisdictional claims in published maps and institutional affiliations.

Electronic supplement

Delayed subsidence of the Dead Sea shore due to hydro-meteorological changes

S. Vey[+, 1], D. Al-Halbouni [1,2], M. Haghshenas Haghighi [3], F. Alshawaf [1], J. Vüllers [4], A. Güntner [1,5], G. Dick [1], M. Ramatschi [1], P. Teatini [6], J. Wickert [1,7], M. Weber[1, 5]

+Corresponding author, e-mail: sibylle.vey@gfz-potsdam.de

[1] Deutsches GeoForschungsZentrum, Potsdam, Germany

[2] GEOMAR – Helmholtz Centre for Ocean Research Kiel, Germany

[3] Leibniz University Hannover, Germany

[4] Karlsruhe Institute of Technology, Karlsruhe, Germany

[5] University of Potsdam, Germany

[6] University of Padova, Italy

[7] Technische Universität Berlin, Germany

Sibylle Vey

GFZ

Telegrafenberg

14473 Potsdam

Germany

GNSS analysis

a) Positioning

The GNSS data analysis for positioning has been performed with the GFZ Earth Parameter and Orbit determination System (EPOS) software [1, 2] which is based on a least squares adjustment of un-differenced phase measurements and adheres to IERS Conventions [3]. A linear combination of the L1 and L2 GNSS observations are used in EPOS software to eliminate the first-order ionospheric effects. For estimation of station coordinates we used the Precise Point Positioning (PPP) strategy [4]. The main idea of the PPP strategy is the processing of each site separately, fixing the high quality GNSS orbits and clocks. Thus, the GNSS data processing splits into two steps. The first processing step includes an estimation of high accurate GNSS orbits and clocks from a global GNSS network. In this step we used about 100 globally distributed stations of the International GNSS Service IGS. Official products of the GFZ IGS Analysis Centre such as Earth Orientation parameters, GNSS orbits and clocks, have been taken as initials. We used GNSS data with a sampling rate of 2.5 minutes in 24-hour data windows and applied a cut-off elevation angle of 7 degrees. As reference frame the International Terrestrial Reference Frame ITRF2014 has been used. In the second step – PPP analysis – we performed daily estimation of GNSS station coordinates using fixed orbits and clocks of GNSS satellites from the first step. The main advantage of this strategy is the possibility of investigations of site-dependent effects, which was very important in the case of Dead Sea.

b) Reflectometry

The DS lake level (*DSL*) is calculated using the GNSS antenna height *H* from positioning and the height of the GNSS antenna above the reflecting surface *h_refl*

$$DSL=H-h\_refl \quad (1).$$

The reflector height of the GNSS antenna can be derived from the GNSS signal strength [5, 6, 7, 8]. The GNSS signal power is measured as signal-to-noise ratio (SNR) and recorded as standard observation in the Receiver Independent Exchange Format (RINEX) files [9]. The SNR from the Javad receiver has a precision of 0.05 dB. The GNSS data have a sampling rate of 1 s. The reflector height can be estimated from the interference pattern of the signal to noise ratio. By subtracting a second order polynomial from the SNR data the interference pattern was isolated. The amplitude of the SNR, given in logarithmic dB-Hz units, was converted into the linear volts/volts. The SNR interference pattern is a function of the satellite elevation angle E and shows a periodic signature. Assuming a locally planar and horizontal surface the frequency f of the multipath pattern is constant when $\sin(E)$ is used as independent variable [10]. The frequency $f = \frac{4\pi h}{\lambda}$ of the interference pattern depends on the height h of the GNSS antenna above the reflecting surface and on the wavelength λ of the GNSS signal. The frequency of the interference pattern was calculated with the Lomb-Scargle periodogram method [11]. This algorithm calculates the spectral power for irregularly spaced time series. Reflections from elevation angles ranging between 2 deg and 30 deg were used. Satellite tracks, which contain less than 2.000 data points (equal to roughly 30 minutes of observation), were discarded.

The maximum peak in the spectral analysis of the GNSS signal strength was converted into the height of the GNSS antenna above the reflecting surface (Fig. S_1).

The reflector height over the DS lake level increases by 95 cm/y **(**Fig. S_2b). Adding to this the subsidence of the GNSS beach station of 15 cm/y, the DS lake level, derived from GNSS, drops by -110 cm/y (Fig. S_2c). The offsets in the time series due to the relocation of the GNSS station were corrected using height difference calculated from the average antenna height of the 7 days before and after the displacement. The reflection of the GNSS signal from land shows a constant reflector height **(**Fig. S_2d). This means the GNSS station / weather tower (Fig. 1) is not sinking locally but that the subsidence of the GNSS station is a larger scale phenomenon.

The reflection area of the GNSS signals corresponds in first order to an ellipse, which can be described by the first Fresnel zone

$$a = \frac{b}{sinE}; b = \sqrt{\frac{\lambda h}{sinE} + \left(\frac{\lambda}{2sinE}\right)^2} \quad (2),$$

where *a* represents the semi-major axis and *b* the semi-minor axis, λ the GNSS wavelength, *h* the height of the antenna phase center above the reflecting surface and *E* the satellite elevation angle [12].

For our GNSS antenna with a reflector height of 4.6 to 5.6 m the first Fresnel zone has a typical dimension of 50 x 4 m (mayor/minor axis) for a reflection angle "*E*" of 5 deg and 15 x 3 m for a reflection angle of 10 deg, respectively. Most of the signal comes from reflections between 5 deg and 10 deg. Hence, the area covered by the reflections of one satellite, is approx. 70 x 7 m. In this study, we combine the reflections of three satellites, which then cover an area, a "footprint", of about 70 x 20 m.

E (deg.)	**major axis (m)**	**minor axis (m)**
2	200	7
5	50	4
10	15	3
15	8	2

Table 1: Size of GNSS reflectometry footprint (ellipse) as function of reflection angle *E*.

InSAR analysis

We assess the surface displacement around the DS basin by InSAR analysis of 257 images acquired by Copernicus Sentinel-1 SAR sensor between 2014 and 2020. The dataset has a spatial resolution of 20 x 5 m and is acquired during descending passes in the period between October 2014 and April 2020. The temporal resolution of data is 12 days in the period from October 2014 to September 2016 and afterwards it improves to a 6 days repeat cycle. The SAR images are cropped to cover an area of 5 × 2 km centered on 31°25'56"N, 35°23'34"E and then they are co-registered to a common reference image.

For InSAR time series analysis, first, a network of Small Baseline (SB) interferograms [13] was formed. To preserve the interferometric coherence in the rapidly deforming areas, temporal baselines are kept short and each image is connected to the next two consecutive images. A digital elevation model from Shuttle Radar Topography Mission data with a spatial resolution of 90 × 90 m [14] was used to reduce the Earth's reference and topographic phases from the interferograms.

In the next step of InSAR time series analysis, a temporal analysis of both amplitude and phase [15,16] is performed on the network of interferograms to identify the point candidates with high signal to noise ratio i.e. stable phase measurement in time. The candidates are selected in the first iteration such that the amplitude dispersion index is below a threshold value of 0.6. Then, the interferometric phase measurements of these

candidates are statistically analyzed to improve the selection. The final number of points with stable phase measurement in time identified within the area of interest exceeds one hundred thousand.

Once InSAR points with high signal to noise ratio are identified, their interferometric phases are unwrapped and connected in time to estimate the time series of displacement. Finally, phase errors from atmospheric delays are reduced from the time series by spatial and temporal filtering.

The final InSAR measurements are in the satellite's Line of Sight (LOS). Assuming the horizontal displacement is not significant, 1-D LOS measurement d_{LOS} is converted to vertical displacement, d_v, by $d_v=d_{LOS}/\cos(\text{theta})$ where theta~=43° is the incidence angle of the sensor in the study area.

The density and distribution of the InSAR points is high in Sentinel-1 results and the subsidence is reliably retrieved. The results in Figure S_4a show surface deformation in LOS near the Ein Gedi area with a distinct displacement along the shoreline, compare also to [17]. To the Southwest of the Beach station, a maximum LOS displacement of about 18 cm/y away from the satellite is estimated from Sentinel-1. Assuming the horizontal displacement is not significant, the vertical displacement rate in this area is as high as 25 cm/y. The displacement rate at the closest InSAR point to SPA station is 1.5 cm/y in LOS away from the satellite with respect to the arbitrary InSAR reference point (Figure S_4a), equivalent to 2 cm/y of subsidence. The area near Beach station exhibits a displacement of approximately 7.4 cm/y in LOS away from the satellite, which corresponds to 10.1 cm/y subsidence.

The area close to Ein Gedi (SPA and Beach 1, 2, and 3 GNSS stations) are homogenously covered by InSAR measurement points making it possible to compare the InSAR time series of the surface displacement with GNSS data.

Soil mechanics

We consider here a simple 1D-soil compaction theory based on [18, 19] under the following assumptions: The Beach station is located on the clayey marl (lime-carbonates) deposits of the former Dead Sea lakebed. An unconfined, isotropic, homogeneous, fully saturated Dead Sea brine layer of marl of H = 20 m thickness is overlying a thick Holocene salt layer. The depth of this salt layer has been determined by various studies on the Western side of the Dead Sea [e.g. 20]. The salt layer is mechanically stiffer than the marl [21] and therefore we consider only compaction of the Marl layer subject to be relevant for the immediate pore pressure changes. With incompressible fluid and soil particles, under small strains and Darcy's law valid in all hydraulic gradients, we can use the 1D compaction theory to calculate primary consolidation based on a hydraulic head change of $\Delta h = 1.1\,m$ (the mean annual decline of the DS water level, see Fig. 4b)

$$S_p = \frac{C_c * H}{1+e_0} \log\left(\frac{\sigma_0' + \Delta\sigma'}{\sigma_0'}\right) \quad (3).$$

The following parameters are derived from laboratory soil consolidation tests [22, 23] for the Dead Sea lime carbonates: $e_0 = 1.0$, the initial void ratio, yielding a high porosity of n = 0.5 typical for marl sediments above the salt layer and $C_c \approx 0.3 - 0.5$ as the compression index. With $\rho_{LC} = 2750\,kg/m^3$, the density of lime-carbonates and $\rho_{DS} = 1240\,kg/m^3$ the density of Dead Sea brine, the effective stress $\sigma_0' = 270\,kPa$ and effective stress change $\Delta\sigma' = 13.38\,kPa$ due to lowering of the water table can be

calculated. This yields a primary consolidation of $S_p \approx 6.3 - 10.5\ cm$ for both limits of the compression index, respectively. To determine t_{95}, the time after which 95 % of the consolidation of the soil has happened, we use the time dependency formulation based on the solution of the pore pressure diffusion equation [e.g. 24]

$$t_{95} = \frac{(H/N)^2 * T}{C_v} \quad (4).$$

Here, for two drainage faces (N=2) and T = 1.129 the time factor [19] after 95% of consolidation, the coefficient of consolidation C_v plays a crucial role. For the Dead Sea lime-carbonates this value has shown a range over more than 3 orders of magnitude [22] depending on the Atterberg limits of solid plasticity and liquid limit. We here assume values of $C_v = 1.0 - 3.0$. With these parameters, the time needed for 95% primary consolidation is $t_{95} = 1{,}19 - 3.58\ yr$. For a high coefficient of consolidation (C_v = 3.0) we therefore receive a primary consolidation time of roughly 14 months for the 20 m thick marl layer.

Also, secondary consolidation occurs due to plasticity and creep of the clay. Several parameters need to be defined for the following equation

$$S_s = \frac{H}{1+e_0}\ C_\alpha \log\left(\frac{t}{t_{95}}\right) \quad (5).$$

C_α is the secondary compression index and is usually estimated by the change of void ratio over time. It can be assumed to be time independent for low t/t_{95} ratios as common in field measurements. Especially, without vertical drainage and when the final effective stress is in the range of the primary effective stress, C_α/C_C is very low and secondary consolidation is insignificant [19]. However, for our problem this is unlikely as for inorganic clays and silt $C_\alpha = 0.05 * C_C$, and thus C_α is in the range of $0.015 - 0.025$.

Hence, the magnitude after an additional year of compaction ($t = t_{95} + 12\,month$) lies between $S_s \approx 3.9$ and $6.5\,cm$ respectively. As it lies in the same order as the primary consolidation, secondary consolidation is not negligible for the Dead Sea mud.

Given the ongoing decline of the Dead Sea lake level, we assume that primary and secondary consolidation occur continuously at this location and, thus, we simply sum both solutions and receive a range of lime-carbonate soil compaction.

The delay between land displacements at the Beach site and the seasonal fluctuation of the DS level (Fig. 4a) can be explained by considering the influence of the latter on the groundwater pressure distribution.

The description the water table motion in a beach is a classical hydrogeologic problem. Specifically, the residual sea level fluctuation can be viewed as a long-term tide characterized by an amplitude $\zeta_0 = 15$ cm and a period $t_0 = 365$ days.

A preliminary analysis can be carried out through a number of analytical solutions proposed for simplified geometry, geological setting, and tidal signal [21,25]. In the simplest condition, which suffices in the context of the present work to explain the observations, let's consider a homogeneous beach characterized by an isotropic permeability K and effective porosity n_e. The groundwater flow is assumed essentially horizontal so that the pressure distribution is hydrostatic (Dupuit's assumption). Therefore, the governing equation for the water table height ζ above the mean sea level is (Bouissinesq's equation):

$$\frac{\partial \zeta}{\partial t} = \frac{K}{n}\frac{\partial}{\partial x}\left(\zeta \frac{\partial \zeta}{\partial x}\right) \quad (6).$$

With an almost vertical beach, a sea level fluctuation characterized by a simple harmonic motion $\zeta = \zeta_0 \sin\omega t$ with a tidal period $t_0 = 2\pi/\omega$ and a small tidal amplitude (i.e., ζ_0 much smaller than the aquifer thickness), and imposing $\zeta = 0$ at an infinite distance x from the shoreline, the solution of the above equation reads:

$$\zeta(x,t) = \zeta_0 \sin(\omega t - kx)e^{-kx} \quad (7).$$

where the wave number $k = \sqrt{\frac{n_e\omega}{2K}}$. The wave amplitude h_{max} and the time lag t_L of the water table oscillation at a distance x from the shoreline are:

$$\zeta_{max} = \zeta_0 e^{-kx}$$

$$t_L = x\sqrt{\frac{t_0 n_e}{4\pi K}} \quad (8).$$

We consider that the clayey marl deposits of the former Dead Sea lakebed is characterized by $n_e = 0.5n = 0.25$ and $K = 10^{-5}$ m/s because of the fast dissolution and erosion that typically affect the deposits. The shortest distance x of the Beach station from the shoreline changed over time because of the DS level lowering. It ranged approx. from 10 to 35 m. Introducing these values in the previous equation yields $t_L =$ 29 days and $t_L = 101$ days, respectively.

Notice that $\zeta_{max} = 9.0$ cm at x=10 m and $\zeta_{max} = 2.6$ cm at x= 35 m distance, i.e. 60% and 17% of ζ_0, respectively.

Figures - Electronic supplement:

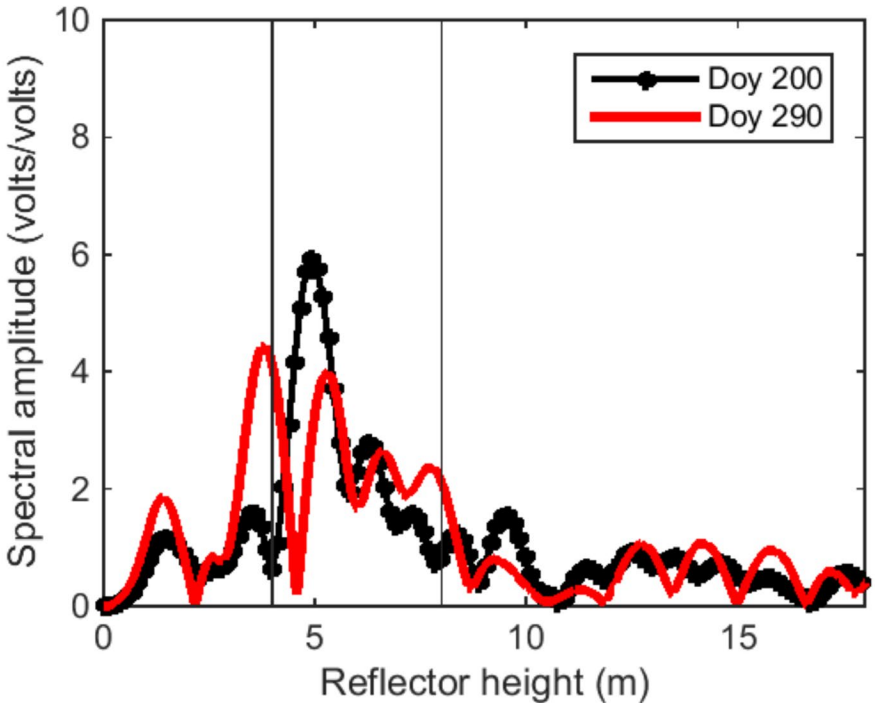

Fig. S_1:

Lomb-Scargle periodogram from the Signal-To-Noise Ratio of the GPS satellite #26. On day 200 (black line) the maximum peak at 4.9m corresponds to the reflector height over the Dead Sea. On day 290 (red line) the standard algorithm would detect the reflector height over the lake at the maximum peak of 3.8m. However, due to the strong horizontal retreat of the DS, this peak corresponds to the reflections from land. The second largest peak at 5.2 m characterizes the reflections from the DS. Our new algorithm uses a window function for the maximum peak detection shown by the vertical lines.

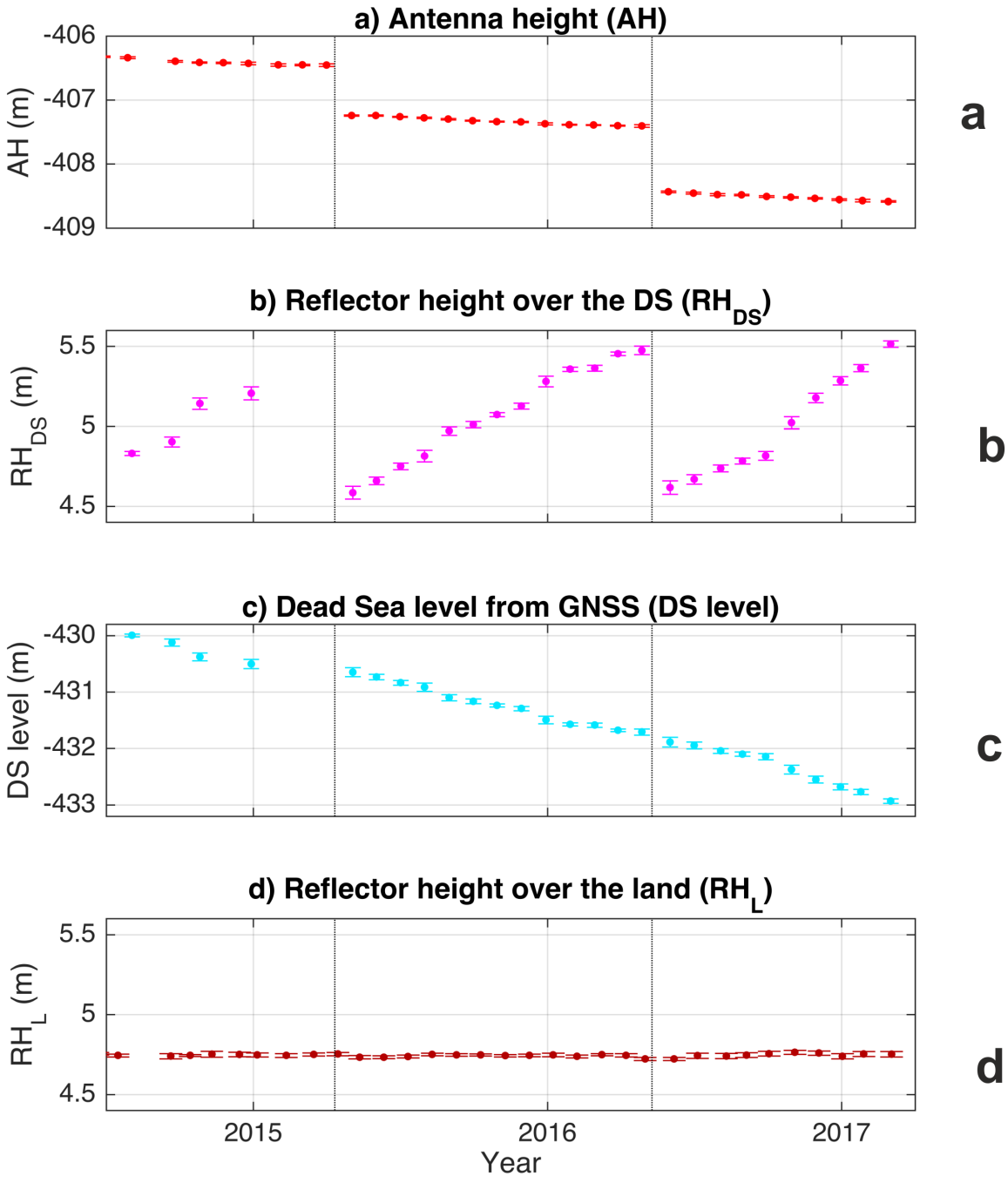

Fig. S_2:

(a) Changes in antenna height from GNSS (red). The station was moved closer to the lake on 10th of April 2015 and again on 9th of May 2016 (dotted vertical lines). The small data gap in 2014 is due to missing observations. **(b)** Reflector height over water

(magenta) is increasing with time corresponding to the drop of the lake level. The gap in the time series is because the water moved to far away from the station for a reliable determination. **(c)** DS lake level (blue) derived from the difference of GNSS antenna height (corrected for the offsets due to the displacements) and the reflector height over water. **(d)** Reflector height over land (brown). This shows that the GNSS station is stable and not sinking into the ground. Error bars in all subplots indicate the standard deviation of the monthly averages based on daily values.

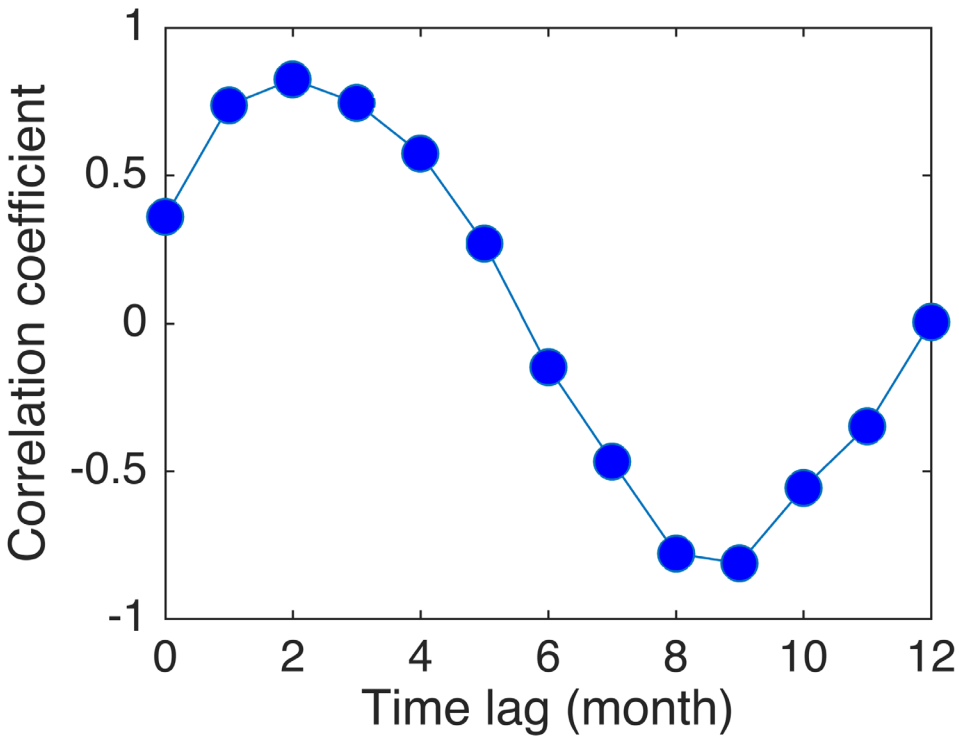

Fig. S_3:

Correlation between the time series of the DS lake level and the subsidence at Beach stations on a monthly basis for different time delays at the Beach station(s). The maximum value of 0.84 is reached for a time shift of 2 months.

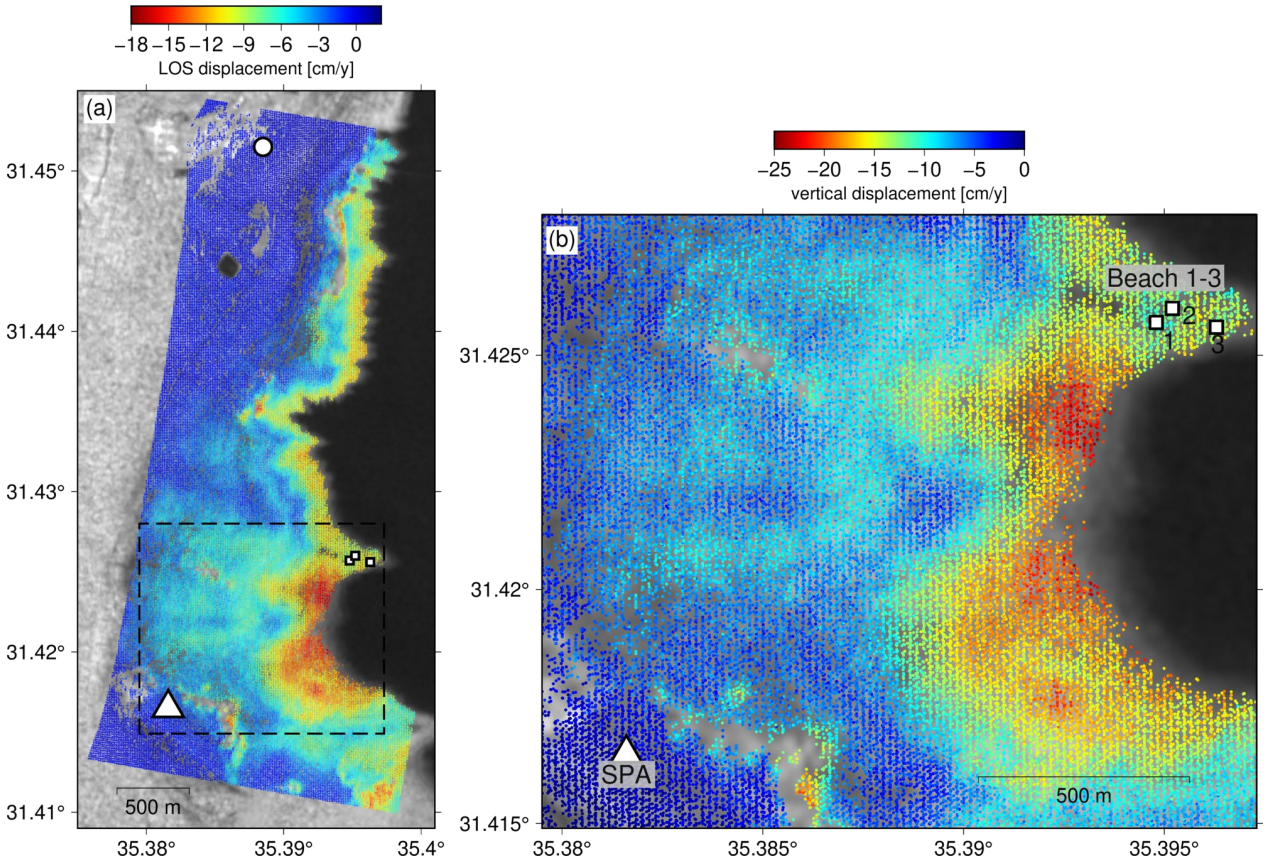

Fig. S_4:

InSAR-based maps of surface displacement rate obtained from SBAS time series analysis of 2014-2020 data from Copernicus Sentinel-1 © ESA overlaid on average SAR amplitude image **(a)** Line of Sight rate of displacement. Dashed line indicates the close up view displayed in (b). **(b)** vertical displacement rate in a close up view for the region near Ein Gedi. The vertical displacement values are estimated assuming horizontal displacements are negligible. The location of the SPA GNSS station is displayed by a white triangle. Beach 1-3 stations are indicated by white squares. The white circle represents the arbitrary spatial reference point for InSAR.

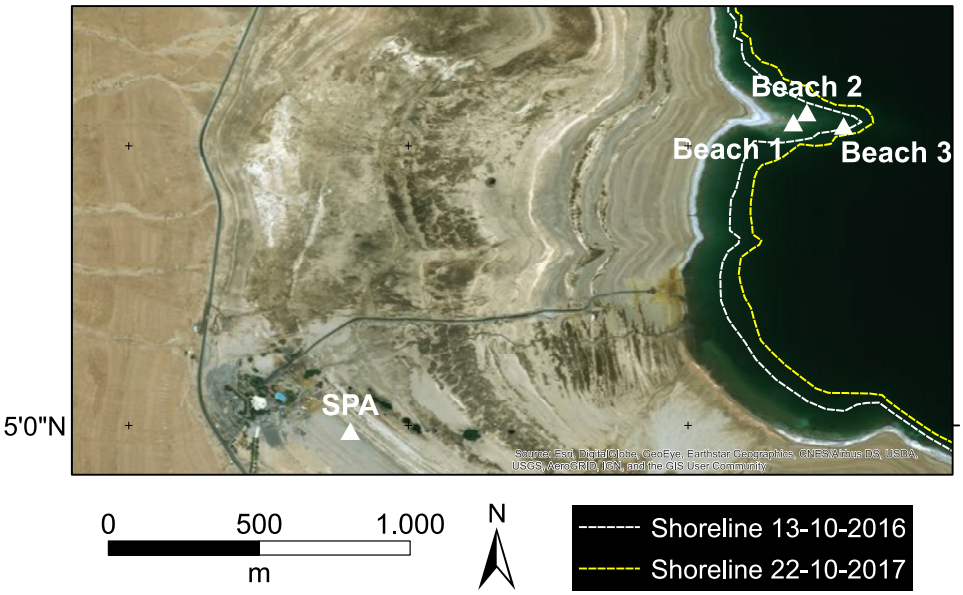

Fig. S_5c:

Background image (DigitalGlobe) from 14th August.2013 with a resolution of 50 cm. Shorelines are extracted from 10 m resolution Sentinel 2 (2016) and 3 m resolution Rapideye (2017) images, respectively.

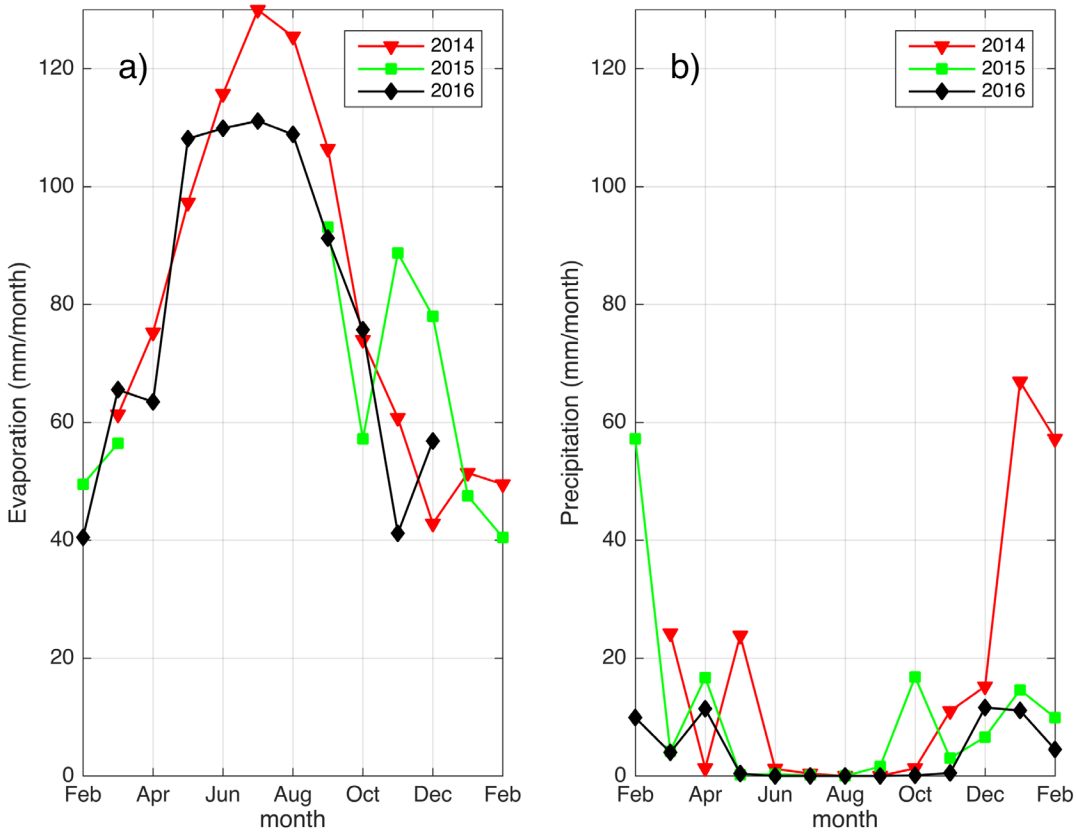

Fig. S_6:

(a) Monthly sum of evaporation at the Beach station (Fig. 1) derived from [26], our basis for the cumulative values in Fig. 4b. **(b)** Monthly sum of precipitation observed at the Beach station. Strong precipitation in winter 2014/15 produces a small increase in the lake level of the DS (Fig. 4b, blue triangles).

References

1. Ge, M., Gendt, G., Dick, G., & Zhang, F. Improving the carrier phase ambiguity resolution in global GPS network solution. *Journal of Geodesy*, 79, 103-110, DOI: 20.2007/s00290-005-0447-0 (2005).

2. Ge, M., Gendt, G., Rothacher, M., Shi, C., & Liu, J. Resolution of GPS Carrier Phase Ambiguities in Precise Point Positioning (PPP) with Daily Observations, *Journal of Geodesy*, 82(7), 389-399, DOI:10.1007/s00190-007-0187-4 (2008).

3. Petit, G. & Luzum, B. (eds.) IERS Conventions 2010, *IERS Technical Note*; 36, Frankfurt am Main: Verlag des Bundesamts für Kartographie und Geodäsie (2010).

4. Zumberge, J. F., Heflin, M. B., Jefferson, D. C., Watkins, M. M., & Webb, F. H. Precise point positioning for the efficient and robust analysis of GPS data from large networks, *Journal of Geophysical Research*, 102, B3, 5005-5017 (1997).

5. Santamaría-Gómez, A. & C. Watson, C. Remote leveling of tide gauges using GNSS reflectometry: Case study at Spring Bay, Australia. *GPS Solutions*, 21(2), 451-459. https://doi.org/10.1007/s10291-016-0537-x (2017).

6. Larson, K. M., Ray, R. D. & S.P. Williams, S. P. A ten year comparison of water levels measured with a geodetic GPS receiver versus a conventional tide gauge. *J. Atmos. Ocean Tech,* Vol. 34(2), 295-307. doi: 10.1175/JTECH-D-16-0101.1 (2017).

7. Frydman, S., Charrach, J. & Goretsky, I. A geotechnical study of evaporitic, lacustrine sediments in the saline environment of the Dead Sea area. *Engineering Geology*, 181, 309-322, doi:10.1016/j.enggeo.2014.08.028 (2014).

8. Strandberg, J. T., Hobiger, T. & Haas, R. Improving GNSS-R sea level determination through inverse modeling of SNR data. *Radio Sci.*, 51, 1286–1296. https://doi.org/10.1002/2016RS006057 (2016).

9. Gurtner, W. & Estey, L. RINEX: The receiver independent exchange format version 2.11. http://igscb.jpl.nasa.gov/igscb/ data/format/rinex211.txt (2007).

10. Larson, K., Small, E., Gutmann, E., Bilich, A., Braun, J. & Zavorotny, V. Use of GPS receivers as a soil moisture network for water cycle studies. *Geophysical Research Letters*, 35(24), L24 405. doi:10.1029/2008GL036013 (2008).

11. Press, W. H. & Rybicki, G. B. Fast algorithm for spectral analysis of unevenly spaced data. *Astrophysical Journal*, 338, 277–280. doi:10.1086/167197 (1989).

12. Larson, K.M. & Nievinski, F.-G. GPS snow sensing: results from the EarthScope Plate Boundary Observatory. *GPS Solution*, 17, 41–52. doi:10.1007/s10 291–012–0259–7 (2012).

13. Berardino, P., et al. A new algorithm for surface deformation monitoring based on small baseline differential SAR interferograms. *IEEE Transactions on geoscience and remote sensing*, 40.11, 2375-2383 (2002).

14. Farr, T. G. & Kobrick, M., Shuttle Radar Topography Mission produces a wealth of data. *Eos, Transactions American Geophysical Union,* 81.48, 583-585 (2000).

15. Hooper, A., A multi-temporal InSAR method incorporating both persistent scatterer and small baseline approaches. *Geophysical Research Letters,* 35.16 (2008).

16. Hooper, A., Segall, P. & Howard Zebker, H. Persistent scatterer interferometric synthetic aperture radar for crustal deformation analysis, with application to Volcán Alcedo, Galápagos." *Journal of Geophysical Research: Solid Earth* 112.B7 (2007).

17. Nof, R. N., M. Abelson, E. Raz, Y. Magen, S. Atzori, S. Salvi & Baer, G. SAR interferometry for sinkhole early warning and susceptibility assessment along the Dead Sea, Israel, *Remote Sens.*, *11*(1), 89, doi:10.3390/rs11010089 (2019).

18. Terzaghi, K., *Theoretical Soil Mechanics*, John Wiley & Sons, New York (1943).

19. Terzaghi, K., Peck, R.B. & Mesri, G. *Soil mechanics in engineering practice*, John Wiley & Sons (1996).

20. Shalev, E. & Lyakhovsky, V. Viscoelastic damage modeling of sinkhole formation, *J. Struct. Geol.*, *42*, 163–170, doi:10.1016/j.jsg.2012.05.010 (2012).

21. Carr, P. A. & Van der Kamp, G. S., Determining aquifer characteristics by the tidal method, *Water Resources Research*, 5(5), 1023-1031 (1969).

22. Ezersky, M. G. & Frumkin, A. Fault - Dissolution front relations and the Dead Sea sinkhole problem, *Geomorphology*, *201*, 35–44, doi:10.1016/j.geomorph.2013.06.002 (2013).

23. Ismeik, M., Ashteyat, A.M. & Ramadan, K.Z. Stabilisation of fine-grained soils with saline water, *Eur. J. Environ. Civ. Eng.*, *17*(1), 32–45, doi:10.1080/19648189.2012.720399 (2013).

24. Verruijt, A. Soil Mechanics. Delft University of Technology (2012).

25. Nielsen, P., Tidal dynamics of the water table beaches, *Water Resources Research*, 26(9), 2127-2134 (1990).

26. Gräbe, A., T. Rödiger, K. Rink, T. Fischer, F. Sun, W. Wang, C. Siebert & Kolditz, O. Numerical analysis of the groundwater regime in the western Dead Sea escaprment, Israel + West Bank, *Environ. Earth Sci.*, *69*, 571–585, doi:10.1007/s12665-012-1795-8 (2013).